Chapter

Physical and Mechanical Properties of Herrnholz Granite: An Ideal Experimental Material

Ying Li and Rui Wu

Abstract

Granite, as the most common plutonic rock of the Earth's crust and the most widely used paving block and building stone in industrial activities, has been widely employed in experimental investigations on its chemical composition, physical properties, and mechanical responses. This chapter focuses on the physical and mechanical properties of Herrnholz granite while emphasizing that it is an ideal experimental material for its homogeneity and fine-grained nature. Among the properties discussed here are density, porosity, pore size distribution, ultrasonic wave velocities, strength, fracture toughness, and hydroscopic/hygroscopic properties. Preliminary laboratory data sets to reveal relationships between the hygroscopic properties and mesoporous character of the Herrnholz granite as a result of water adsorption on internal fabric elements, such as pores, and microcracks.

Keywords: Herrnholz granite, fine-grained nature, homogeneity, mesoporous media, mechanical response, hygroscopic expansion

1. Introduction

Granite is the most common plutonic rock of the Earth's crust and has been used for a variety of rock engineering and geomechanical purposes, including underground disposal of radioactive waste (e.g., see [1–3]), cavern construction for liquid natural gas or liquid petroleum gas storage (e.g., see [4, 5]), and geothermal energy extraction from hot dry rock (e.g., see [6, 7]). To select a specific site for those geotechnical applications, geological (e.g., geometry, hydrology, and geochemistry), engineering (e.g., stress state, physical, and mechanical properties), and socioeconomic (e.g., seismicity, water, and land resources) conditions are typically taken into account [8–10]. Physical and mechanical properties of the host rock are normally evaluated at a later stage of the site selection process when all other factors are favorable. Granite has also been used as a construction stone, such as building facades, walls, sockets, and sculptures (see [11–14]), due to its abundance, petrophysical properties, durability, and textural uniformity. A detailed examination of the physical and mechanical properties of such granite helps to evaluate its long-term behavior in various building situations and environmental conditions.

The physical and mechanical properties, such as the bulk density, porosity, and uniaxial compressive strength, of a variety of granite have been reported (e.g., [7, 14–21]). In some cases, the ultrasonic velocity test [14, 22–25], the Schmidt hammer test [14, 25, 26], or the absorption test [14, 27–29] were performed, providing insights into the relationships between measured properties, for example, the relationship between UCS and porosity, between UCS and Schmidt rebound hardness, and between ultrasonic velocity and porosity. Note that these studies typically do not include microstructure characterization, such as grain size, grain shape, and pore size distribution, which indeed have been shown to be related to the mechanical and physical response [16, 30–32].

This chapter aims to provide an overall picture of Herrnholz granite by expanding on its microstructural characteristics and physicomechanical properties. For initial microstructure characterization, a series of techniques including optical petrographic and fluorescence (i.e., filling microcracks with a fluorescent dye) microscopy, mercury injection porosimetry, and nitrogen adsorption analysis were employed. Subsequent mechanical properties investigation involved a series of uniaxial compressive strength (UCS) tests and single edge notch bending (SENB) tests. Deformation and elasticity variation of Herrnholz granite in response to a range of relative humidity, referred to as the hygroscopic properties, and to the progressive water imbibition, referred to as the hydroscopic properties, were evaluated under controlled climatic conditions using a unique combination of on-specimen strain, applied load and displacement, and digital image correlation (DIC).

2. Granite studied

Granite studied in this chapter was sourced from the Herrnholz quarry (HQ), east of the Hauzenberg pluton (HP), NNW of Munich, in Germany (**Figure 1a**). The Hauzenberg pluton ($\sim 100\ km^2$ in area), together with the Kristallgranite ($\sim 400\ km^2$ in area) and the Fuerstenstein ($\sim 100\ km^2$ in area) plutons, are commonly located between the Danubian fault and the Bavarian Lode shear zone (**Figure 1b**), and represent the westernmost part of the South Bohemian Massif. Granite in the Hauzenberg pluton was formed during the Variscan orogeny and intruded late-to post-kinematically at $\sim$ 320 Ma (e.g., [33, 34]) within the Moldanubian part of the southwestern Bohemian Massif. Rapid cooling ($100°C/Ma \sim$ for 2–3 Ma) and a single phase of exhumation under relatively consistent tectonic conditions have produced homogeneous granite with minimal to no ductile tectonic overprint, which makes it a popular building stone in the region.

Two hundred samples were cut from a single $0.6\ m^3$ block (**Figure 1d**) of Herrnholz granite for a range of geomechanical laboratory testing. The block showed little to no discoloration or staining, indicating its unweathered nature. All samples were oriented relative to the principle splitting directions, the 'rift', 'grain', and 'hardway'. The rift is the plane along which the granite cleaves with the greatest ease, followed by the grain, and lastly by the hardway. The easiest splitting direction is most likely due to parallel micro-cracks in the homogeneous fine-grained granite, the grain may be determined by inherited mineralogical characteristics (e.g., cleavage of feldspar and mica), or tectonic fractures, and the hardway may be a direction at right angles to the other two.

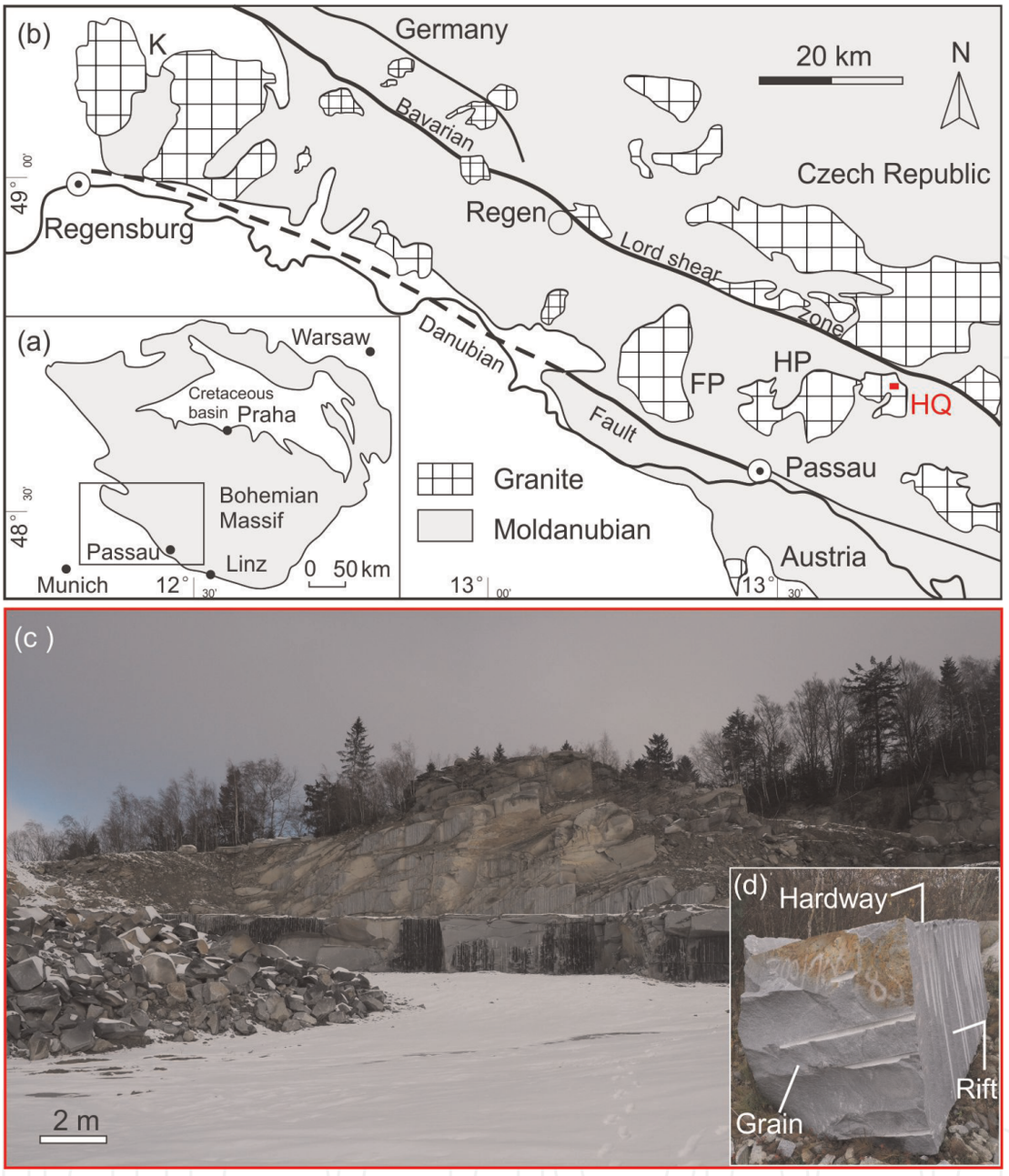

Figure 1.
(a) Map showing the location of the Bohemian Massif; (b) Simplified geological map (modified after Refs. [33, 34]) showing the location of Herrnholz quarry (HQ) with respect to the distribution of three largest granite intrusive plutons in the westernmost part of the South Bohemian Massif: FP, Fuerstenstein Pluton; HP, Hauzenberg Pluton; K, Kristallgranite. (c) Photo of the Herrnholz quarry front; and (d) photo of the selected block for samples preparation, showing rift, grain, and hardway planes.

A suit of 35 mm × 22 mm × 15 mm Herrnholz granite prisms was prepared for thin sections (35 mm × 22 mm, $\sim 30 \pm 5$ μm thick) observation. Biotite grains can be distinguished from others under plane-polarized light by their brownish appearance (**Figure 2a**), while muscovite crystals are distinctive in crossed-polarized light by their mottled appearance with rainbow pattern (**Figure 2b**). Quartz can be distinguished from feldspar because it is generally clear and lacks visible twinnage or cleavage, despite all being shades of dark gray through to white in crossed-polarized light. These observations indicate granitic mineralogical assemblage of our selected

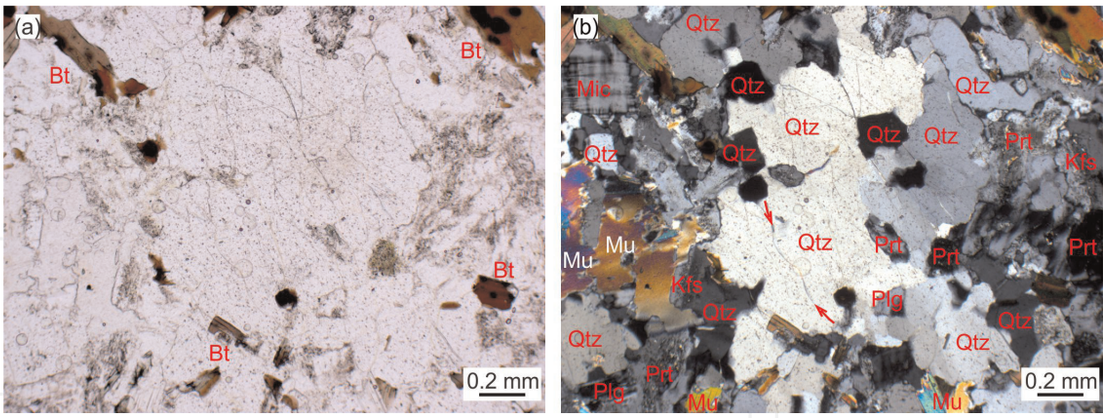

Figure 2.
Petrographic thin section of Herrnholz granite (a) in plane-polarized light, showing biotite (Bt) in brown; (b) in crossed-polarized light, showing interlocking quartz (Qtz), K-feldspars (Kfl) in form of microcline, perthite (Prt), and plagioclase (Plg), all in shades of dark gray through to white, and muscovite (Mu) with rainbow patterns.

specimen, with interlocking quartz (50% in area fraction) and feldspars (38% in area fraction), together with a small portion of mica (11% in area fraction). The grain size, calculated as average length of each grain's longer and shorter axes, is generally between 0.03 and 1 mm, with a mean diameter of 0.23 mm and a standard deviation of 0.13 mm.

3. Methods

3.1 Microstructure observation

Pore spaces (e.g., pores and cracks) within a thin section are hardly detected by microscope examination when not highlighted by iron or other filling minerals (e.g., [15]). A combination of optical petrographic and fluorescence microscopy was therefore employed to characterize the distribution of pore spaces in Herrnholz granite. Thin sections were dyed with a fluorescent pigment, which caused throughgoing pores and cracks to glow neon-green under ultraviolet light. We merged images obtained with crossed-polarized light and ultraviolet light into a single 3.2 Mpx mosaic (**Figure 3**), over which various cracks, for example, grain boundary cracks, intragranular cracks, and intergranular cracks connecting grain boundaries to the inside of grain, were able to be detected. In general, quartz crystals most commonly contain single intragranular or intergranular cracks, while feldspar crystals commonly contain a population of cleavage-parallel intergranular cracks.

Total porosity (ϕ_t), defined as the fraction of bulk volume occupied by the total pore space, can be determined from the difference between the bulk and grain density. Bulk densities (ρ_b) of two oven-dried Herrnholz granite prisms $(25\ \text{mm} \times 25\ \text{mm} \times 40\ \text{mm})$ at a temperature of 80°C for three days ($< 0.1\%$ mass change in 24 h) were calculated as the ratio of oven-dry mass to bulk volume. The masses of these samples were directly measured using an analytical balance (accuracy of 0.001 g), and the volume was determined from vernier caliper (accuracy of 0.01 mm) measured dimensions. Grain densities $\left(\rho_g\right)$ of the same samples were measured using a helium pycnometer (model: AccuPyc II196, the accuracy of 0.02 m^3 in grain volume). After placing the oven-dried sample in a sample cell of known

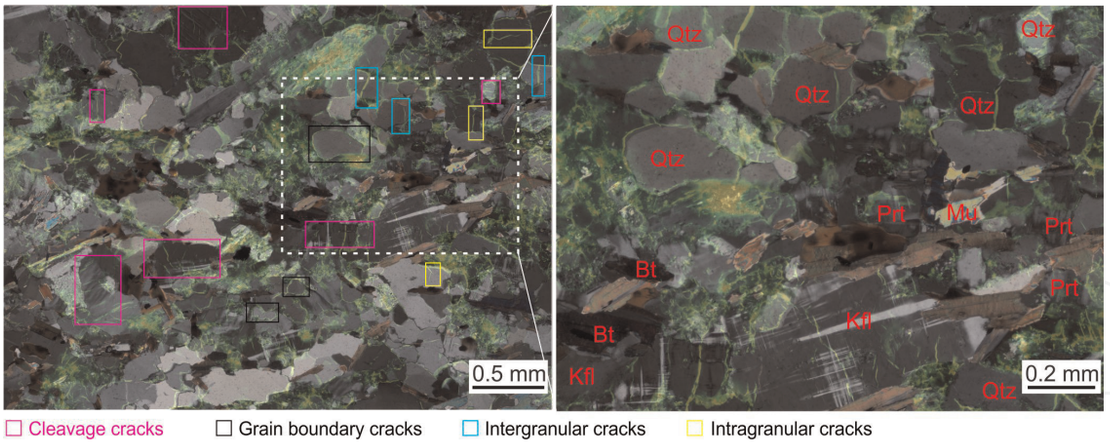

Figure 3.
Superimposed micromosaic obtained with crossed-polarized light and ultraviolet light, indicating regions of (i) cleavage cracks: in straight and parallel patterns within a grain; (ii) grain boundary cracks: along grain boundaries; (iii) intergranular cracks: connecting grain boundaries to the inside of a grain; and (iv) intragranular cracks: within a grain in random or parallel distributed sets (Qtz: quartz; Kfl: K-feldspar; Prt: perthite; Bt: biotite; Mu:muscovite).

volume at an initial pressure, helium gas was admitted to fill the sample cell and the resulting pressure was measured. The grain volume can be calculated from the two measured pressures, the known volume of the sample cell, and the added helium gas using the ideal gas law.

Other pore space properties, including accessible porosity, pore size distribution, and specific surface area of the Herrnholz granite were quantified using a combination of mercury injection porosimetry and nitrogen adsorption analysis. A suite of seven 20 mm × 6.5 mm × 6.5 mm Herrnholz granite prisms was prepared for mercury porosimetry. From measured intrusive volume of mercury under controlled pressures, mercury injection porosimetry can provide information on pore volume or porosity, as well as a wide range of pore throat size (typically from 3 to 10 nm up to microns). The nitrogen adsorption method can evaluate the size of mercury-inaccessible small pores by measuring the amount of adsorbate at a series of relative pressures. To this end, two intact 40 mm × 10.5 mm × 10.5 mm samples were prepared for nitrogen adsorption analysis using an automated gas sorption analyzer, Autosorb iQ™. The existing instrument software AsiQwin™ computed connected surface area and pore size distribution based on the Brunauer-Emmett-Teller (BET) [35] and BarretJoyner-Hallenda [36] model, respectively. The details of these models have been discussed in the mentioned papers; hence, they were not explained here.

3.2 3D ultrasonic tomography

3D ultrasonic tomography on three cuboidal (160 mm × 160 mm × 160 mm) specimens of Herrnholz granite was performed under ambient conditions. Three dimensions of the tested specimens relative to the quarry fabric, that is, rift, grain, and hardway (see **Figure 1d**) were denoted as *G1*, *G2*, and *G3*, respectively. **Figure 4** presents a schematic representation of the ultrasonic tomography setup along the *G1* direction (as an example), in which an array of nine in-house piezoelectric (PZT) transmitter (model: PCT-MCX) [37] and nine passive PZT receivers (model: KRNBB-PC) [38] were mounted on the top and bottom surfaces of the granite cube,

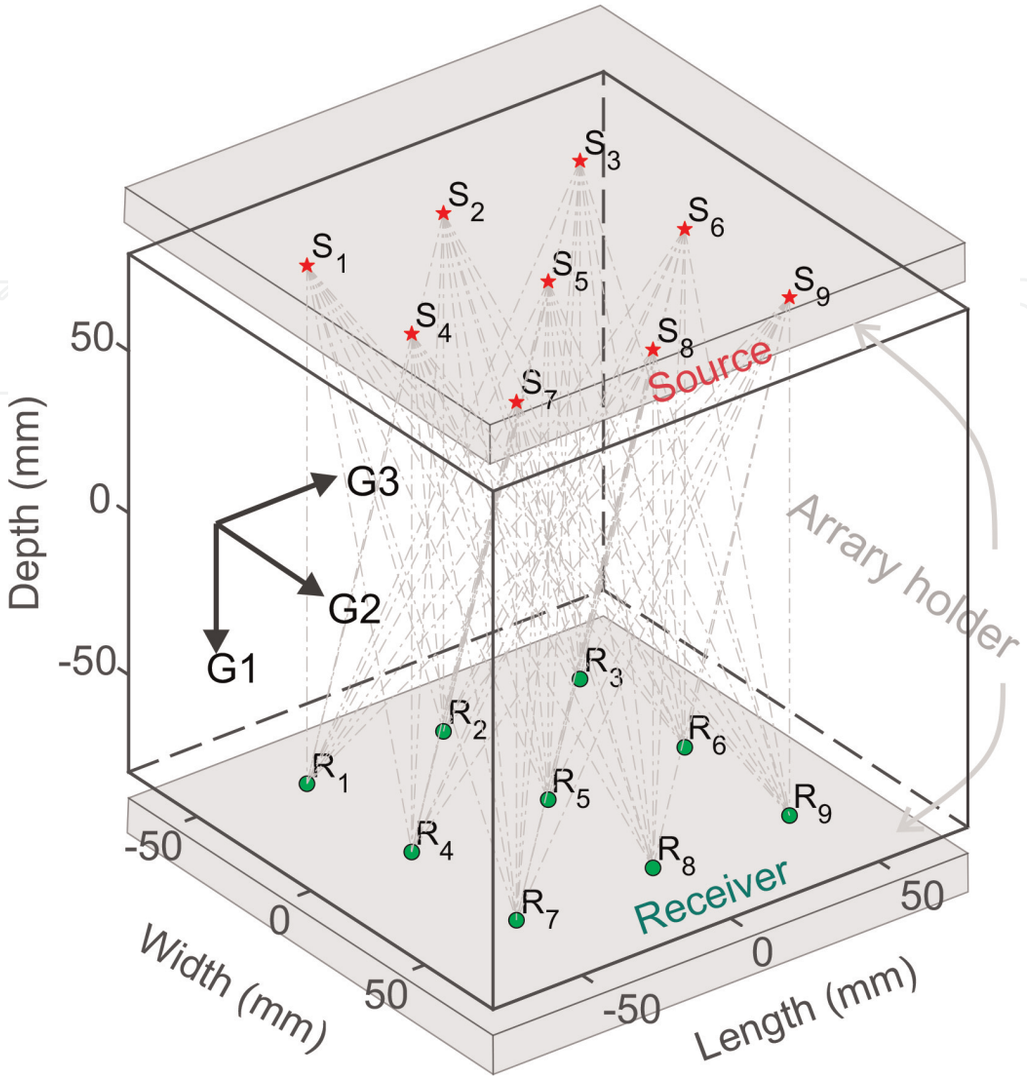

Figure 4.
Schematic representation of ultrasonic tomography setup. G1, G2, and G3 denote the three dimensions relative to the three principle splitting directions, and S and R indicate the Source and Receiver, respectively.

respectively, through two aluminum array holders (gray blocks, see **Figure 4**). A pulsing unit was used to apply a 300 V impulse source, with a duration of 1 μs, to the PZT transmitters. Each transmitter emitted an impulse source in a sequential manner, and the waveforms on nine receivers were recorded by the data acquisition system at a sampling rate of 20 MHz and 16-bit resolution.

Each specimen was modeled as 6 × 6 × 6 cubic elements, each having dimensions of 26.7 mm × 26.7 mm × 26.7 mm, for tomography. As indicated by dashed lines in **Figure 4**, there were 81 straight ray paths (assuming wave propagation by straight rays) that sample most of the elements between the transmitter and receiver planes (i.e., *G*1 planes). The time intervals for the first P-wave arrivals from the transmitters to the receivers and the distance of each transmitter–receiver pair were stored in two 9 × 9 arrays to derive the P-wave velocity array. P-wave velocity structure was derived at the center of each cubic elements using the Moore-Penrose pseudoinverse. More detail and the mathematical description of this inversion problem have been described in Ref. [39]; hence, they were not explained here.

3.3 Rock mechanics laboratory testing

In order to determine elastic and brittle properties of Herrnholz granite, a range of uniaxial compressive strength and single-edge notch three-point bending (also known as three-point bending) tests were performed with a custom static loading frame (see details in Ref. [40]) at the Rock Physics and Mechanics Laboratory, ETH Zurich. With the loading frame, the applied load and piston displacement are directly measured with a load cell and displacement transducer, respectively. Surface strains of a tested sample can be tracked using a range of extensometry products connected to the test machine controller. These include a radial chain extensometer (Epsilon Model 3544) and a four-point averaging longitudinal extensometer (Epsilon Model 3442RA1), which are often employed together in UCS tests to measure radial and axial strains, respectively, of a cylindrical sample as it is compressed (see **Figure 5a**), and a crack mouth opening displacement gauge (Epsilon Model 3541) that can be used directly on a SENB specimen with the knife edges glued to the test specimen or, alternately, with bolt-on knife edges mounted on the test specimen. In order to avoid effects associated with creeping of the adhesives or localized damage during bolt-hole preparation, the crack mouth opening displacement gauge in this study is clamped by knife edges manufactured within an L-shape titanium holders, of which the 8 mm-deep leg is embedded in the notch (> 8 mm deep) of a SENB specimen (see **Figure 5b**).

3.3.1 Uniaxial compressive strength tests

UCS tests were performed on 10 cylinders (50 mm in diameter, 140 mm in height) under ambient conditions to determine elastic properties, for example, Young's modulus (E) and Poisson's ratio (v), and brittle properties that include the crack initiation

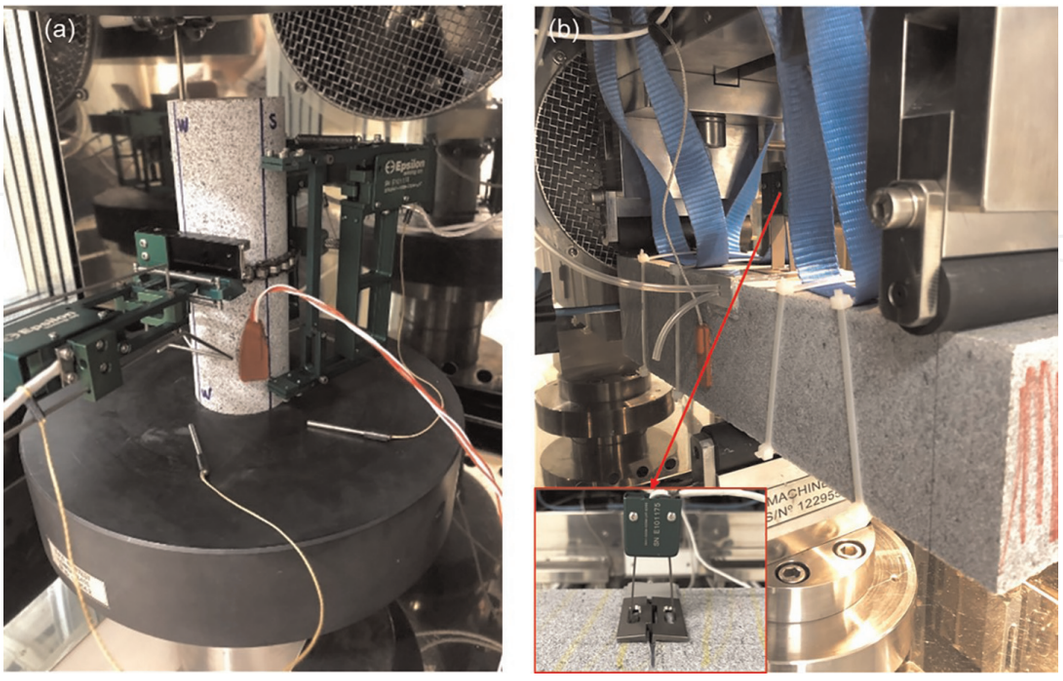

Figure 5.
Setup of uniaxial compressive strength (UCS) and single edge notch three-point bending (SENB) tests with a custom static loading frame at the Rock Physics and Mechanics Laboratory, ETH Zurich. (a) A UCS specimen was mechanically mounted with longitudinal and circumferential extensometers; (b) A SENB specimen was mounted with a knife edges-clamped crack mouth displacement gauge.

(CI) threshold, critical damage (CD) threshold, and UCS of Herrnholz granite. Every specimen was cored in the same direction and ground into two parallel end surfaces. The specimens were loaded at a constant displacement (piston) rate (4 mm/min) to failure, with load and displacement (incl. piston and sample) being logged over the failure process. To minimize the potential of damaging the displacement transducers, the failure of each specimen was arrested by a servo-controlled break detection mechanism that instantaneously unloaded the specimen when the load dropped more than 0.02% of the peak.

Stress–strain curves developed during the failure process were used to determine both the elastic and brittle properties. Young's modulus was determined as the slope of the linear portion of each axial stress–axial strain (σ_a vs. ϵ_a) curve, basically between 20% and 50% of the average UCS. Poisson's ratio was determined by linear regression of the radial strain–axial strain (ϵ_r vs. ϵ_a) curve over the same stress interval. The CI threshold represents the axial stress at which new cracks begin to form and can be determined using the crack volumetric strain reversal method [41, 42]. In this method, the crack volumetric strain (ϵ_{CV}) is calculated using the following formula:

$$\epsilon_{CV} = \epsilon_{vol} - \epsilon_{EV} \tag{1}$$

where ϵ_{vol} is the volumetric strain, assumed to be $\epsilon_a + 2\epsilon_r$,ϵ_{EV} is the elastic volumetric strain and can be calculated by:

$$\epsilon_{EV} = \frac{1-2v}{E}\sigma_a \tag{2}$$

The CD threshold corresponds to the start of unstable crack growth and can be determined by the reversal point in the volumetric strain-axial stress (ϵ_{vol} vs. σ_a) curve.

3.3.2 Single edge notch bending tests

SENB tests were performed on 4 Herrnholz granite beams under ambient conditions to determine their fracture toughness. Every beam is 400 mm long, with a span length between the bearings of 360 mm, a cross-section of 90 × 90 mm, and a 3 mm wide, 9 mm deep saw-cut notch in the outer bending radius. Two of the samples were loaded to failure under load-point displacement (piston) control at a rate of 1 μm/s. The other two samples were subjected to staged loading increases (ranging from 50 % to 98 % of the predetermined peak load) with load-point displacement maintained for up to 30 min between each load stage, aiming to gain insights into the time-dependent behavior of the Herrnholz granite. The fracture toughness of Herrnholz granite can be determined from the measured peak load using the following formula:

$$K_{IC} = \frac{F}{w\sqrt{h}}\left[\frac{3\frac{l}{h}\sqrt{\frac{a}{h}}}{2\left(1+2\frac{a}{h}\right)\left(1-\frac{a}{h}\right)^{\frac{3}{2}}}\left[1.99 - \frac{a}{h}\left(1-\frac{a}{h}\right)\left[2.15 - 3.99\frac{a}{h} + 2.7\left(\frac{a}{h}\right)^2\right]\right]\right] \tag{3}$$

where F is the measured peak load, l is the span length, w and h are the sample width and height, respectively, and a is the initial depth of the notch.

3.4 Water imbibition and adsorption tests

Increases in the water content of intact rock, either through exposure to high ambient humidity, or the addition of liquid water, have been shown to increase strains [27–29, 43] and change mechanical properties [44–49]. To differentiate the conditions that lead to these variations, we refer to them as hygroscopic (when related to humidity changes) and hydroscopic (when related to water immersion and/or imbibition) properties. The hydroscopic and hygroscopic properties of Herrnholz granite were determined through water imbibition experiments on two free-standing 115 × 65 × 35 mm granite prisms, and water vapor adsorption experiments on a single granite cylinder (50 mm in diameter and 140 mm in length) subjected to unconfined compression, respectively.

3.4.1 Liquid water imbibition tests

Water imbibition tests on two 115 × 65 × 35 mm granite prisms were performed with distilled water as the wetting fluid proceeded from the top to the bottom of each specimen as a combined result of gravity and capillary effect. The test arrangement is schematically presented in **Figure 6**, where water was introduced to the upper sample surface through two pieces of 65 mm wide filter paper folded with one end covering the sample surface and the other immersed in a distilled water reservoir ~ 15 mm above the specimen. Aluminum blocks were placed on the filter paper to ensure a positive contact surface between the saturated filter paper and the sample. In order to track the surface deformation of the specimens undergoing gradual wetting, time-lapse photographs were acquired using a combination of Sony Alpha A7RII digital camera and Sony FE 24–105 mm F4 G OSS zoom lens with the sensor plane parallel to the vertical plane (65 × 115 mm) of the tested sample. Digital Image Correlation (DIC) analysis of hundreds of photographs taken over 16–24 h was undertaken in Ncorr software [50]. The details of this software have been discussed in the mentioned papers; hence, they were not explained here.

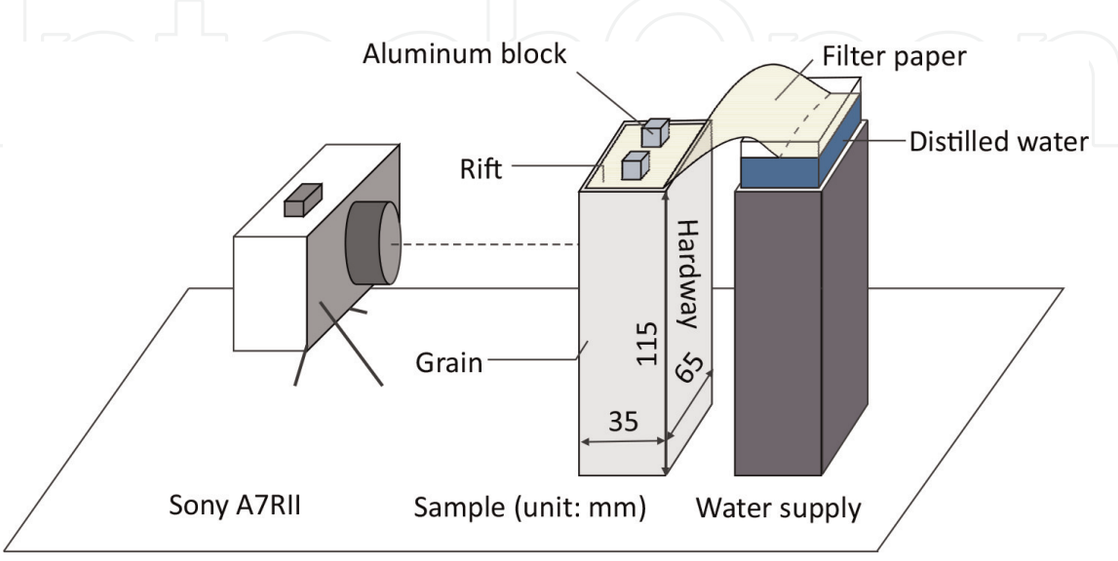

Figure 6.
Schematic diagram of the capillary imbibition experiment on a free-standing 115 × 65 × 35 *mm granite prism.*

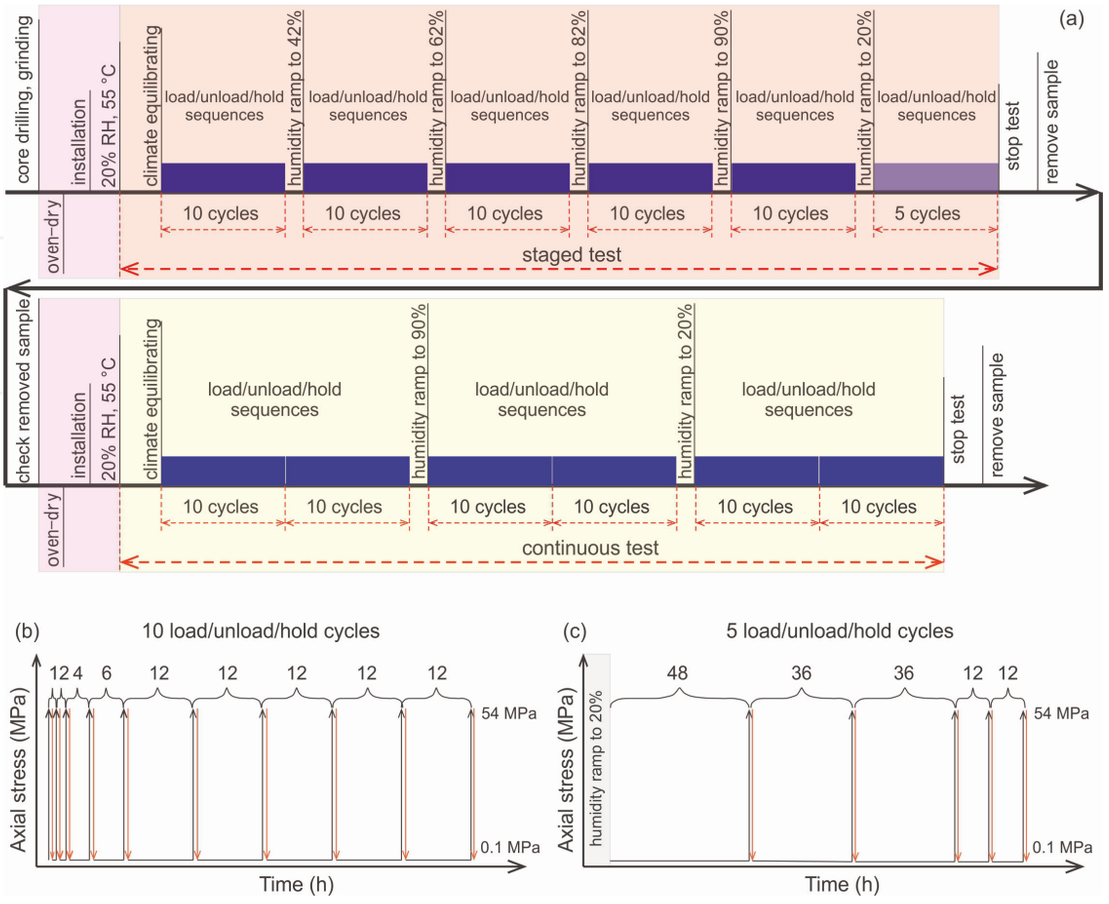

Figure 7.
Flowchart of the "staged" and "continuous" uniaxial compression tests (a), with panels (b and c) illustrating the 10 load/unload/hold cycles and 5 load/unload/hold cycles, respectively.

3.4.2 Water vapor adsorption tests

To derive hygroscopic properties of Herrnholz granite, two uniaxial compression tests on a single Herrnholz granite cylinder (50 mm in diameter and 140 mm in length) exposed to "staged" and "continuous" humidity variation were performed. The first "staged" test employed a humidity stepping protocol, before the sample was removed, checked, oven dried, and prepared for the second test, which employed a "continuous" humidity stepping protocol (see flowchart in **Figure 7a**). The sample was dried in an oven at 80°C for 3 days prior to each test to ensure identical initial moisture conditions and to prevent inadvertent damage to the microstructure. The sample was then transferred to a custom static loading frame with integrated climate chambers [40] and loaded for 1 day with a constant axial stress of 0.1 MPa, 20% humidity, and 55°C to allow the sample to equilibrate. During the staged test, relative humidity was ramped in a stepwise manner from 20 to 42, 62, 82, and 90% before returning to 20%. We increased the relative humidity from 20% to 90% in the continuous test before returning to 20%. In both tests, the axial stress increased at a rate of 1 MPa/s from 0.1 to 54 MPa (the predetermined CI threshold), then decreased at the same rate and remained constant at 0.1 MPa for 1 and 48 h (**Figure 7b** and **c**). Throughout the hold stages, cumulative strains were observed while axial stress was held constant at 0.1 MPa. During the loading stages, axial stress-strain relationships were used to derive elastic properties at each humidity level.

4. Results and discussion

4.1 Density, porosity, and pore size distribution

The mass and volume ratios of three tested specimens indicate an average bulk density of 2.61 g/cm^3, and grain density of 2.664 g/cm^3. Their uncertainties $\left(\frac{\delta\rho}{\rho}\right)$ resulted from the uncertainties in mass $\left(\frac{\delta m}{m}\right)$ and volume $\left(\frac{\delta V}{V}\right)$ measurements and can be evaluated by:

$$\frac{\delta\rho}{\rho} = \sqrt{\left(\frac{\delta V}{V}\right)^2 + \left(\frac{\delta m}{m}\right)^2}. \tag{4}$$

This provides an uncertainty of 0.08% or 0.002 g/cm^3 in the bulk density, and 0.10% or 0.003 g/cm^3 in the grain density.

Total porosity (ϕ_t) was derived from the difference between the grain and bulk density, that is, $1 - \rho_b/\rho_s$, as 1.9%. Its uncertainty $\left(\frac{\delta\phi_t}{\phi_t}\right)$ was given by

$$\frac{\delta\phi_t}{\phi_t} = \frac{1}{\rho_g - \rho_b}\sqrt{\left(\frac{\rho_b}{\rho_g}\delta\rho_s\right)^2 + (\delta\rho_b)^2} \tag{5}$$

and calculated as 0.2%.

The combination of mercury injection porosimetry and nitrogen adsorption analysis provides a wide range of pore size distributions over 3 nm to 100μm (**Figure 8**). The conversion of mercury intrusion pressure to the corresponding pore throat size (i.e., the Washburn equation, 1921) indicates pore throat sizes ranging from 10 nm to 100 μm (see **Figure 8a**). Nitrogen adsorption analysis shows that pores with a diameter smaller than 10 nm account for 80% of the specific surface area, which is averaged at 0.46 m^2/g (see **Figure 8b**) based on the BET model.

The intrusive volume of mercury ranged from 2.63 to 6.17 mm^3/g (mean at 4.22 mm^3/g) at pressures up to ∼ 400MPa (see **Figure 8a**), suggesting an average mercury-accessible porosity of 1.15%. The nitrogen adsorption analysis provides a pore volume of sim 0.5 mm^3/g (or a porosity of 0.14%) over a pore diameter range of 3–10 nm, which, when compared to the pore volume (4.22 mm^3/g) or porosity (1.15%) accessible by mercury, implies that only 1/12 of the small pores are accessible to nitrogen. The cumulative pore volume measured from mercury injection porosimetry (∼ 1.2 mm^3/g) is slightly greater than that from the nitrogen adsorption analysis (∼ 0.8 mm^3/g) over the overlapped diameter range of the two techniques, that is, 10 − 100 nm, indicating a greater differential of pore volume with respect to pore diameter. This slight inconsistency may be due to the nonuniform pore geometry (e.g., wedge-shaped pore) of the analyzed sample [51].

4.2 Ultrasonic wave velocities

3D ultrasonic tomography shows a nearly isotropic P-wave velocity along three directions and a uniform P-wave velocity structure in each plane. **Figure 9a** as an

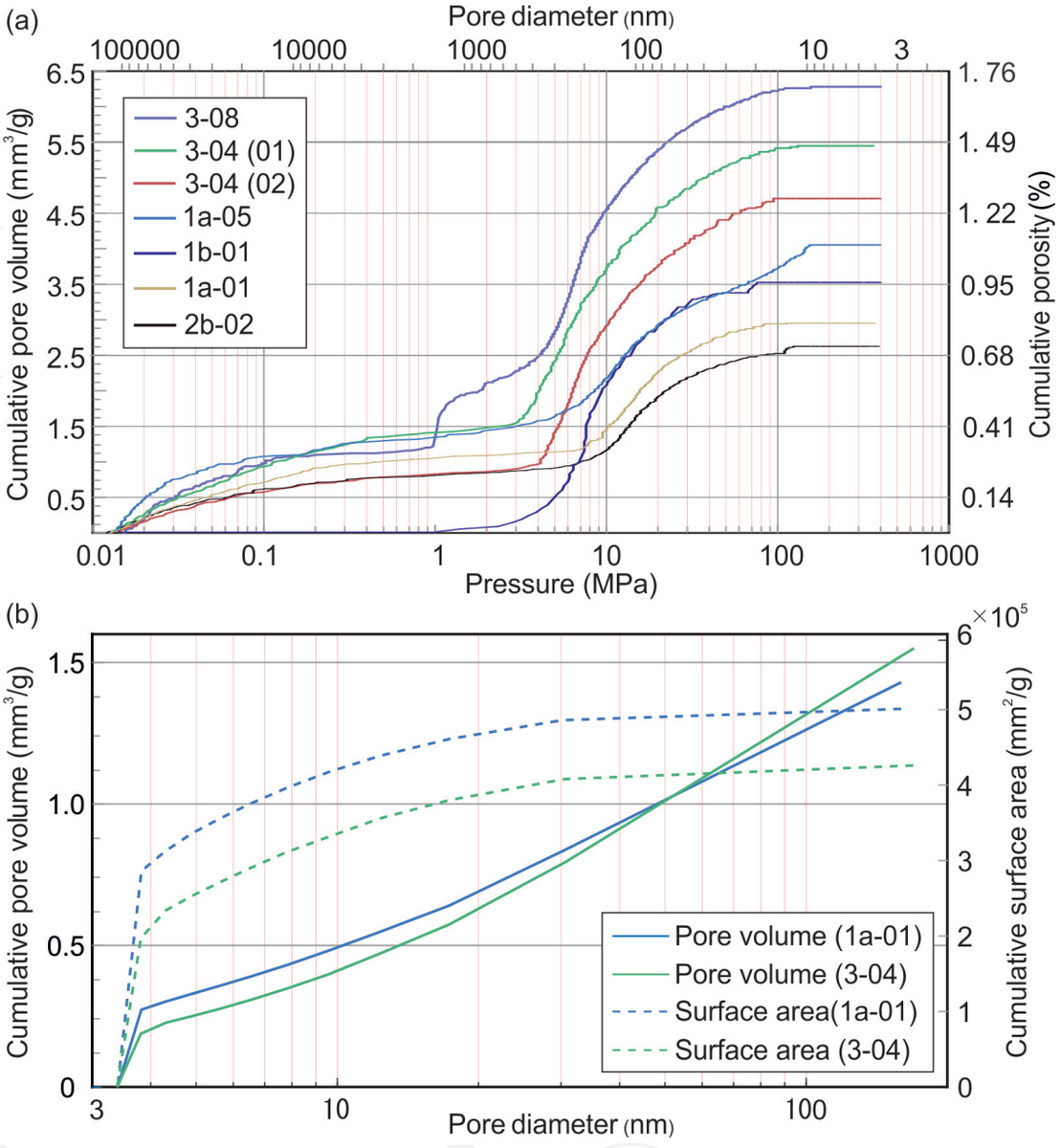

Figure 8.
Comparison of nitrogen adsorption analysis and mercury injection porosimetry results for pore size distribution. (a) Cumulative pore volume and mercury-accessible porosity as a function of pore throat diameter and applied pressure by mercury porosimetry. (b) Cumulative pore volume and surface area as a function of pore diameter during nitrogen adsorption.

example demonstrates the structure of P-wave velocity along the *G1* direction, giving a mean velocity of 3981 m/s, with standard deviation of 68.5 m/s among 64 elements. Note that P-wave velocities of the outermost elements on the *G2* and *G3* surfaces were omitted given the lack of effective coverage of straight rays. P-wave velocities in the *G2* and *G3* direction were similarly characterized, giving 3977 ± 60, and 3988 ± 64 m/s, respectively. Single-peaked normal (or Gaussian) distributions of P-wave velocities in three directions were shown in the probability density functions of **Figure 9b**, with very close peak values (cf. 3997 m/s, 3995 m/s, and 3995 m/s) in three directions. We therefore conclude isotropic wave propagation along three principle splitting directions, and a high degree of homogeneity in P-wave velocity over each plane of the Herrnholz granite. Repeated analysis on the other two specimens was carried on, and the overlapping probability histograms of P-wave velocity

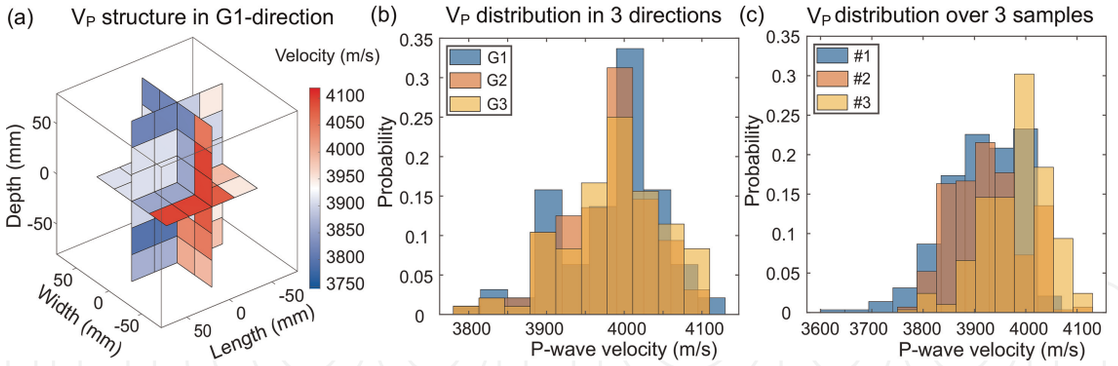

Figure 9.
P-wave velocity tomography of three cuboidal (160 mm × 160 mm × 160 mm) *specimens of Herrnholz granite. (a) P-wave velocity structure in the G1 direction; (b) P-wave velocity histograms along the G1, G2, and G3 directions of one specimen. (c) P-wave velocity histograms for three tested specimens.*

distribution were presented in **Figure 9c**, showing average P-wave velocities of 3914 ± 74, 3925 ± 71, and 3982 ± 64 m/s, respectively, of three tested specimens.

4.3 Elastic properties, brittle properties, and progressive failure characteristics

Axial stress–strain curves (**Figure 10**) derived from ten UCS tests indicate a consistent brittle failure process among ten tested Herrnholz granite cylinders: (i) closure of preexisting cracks prior to a linear stress response; (ii) linear elastic behavior corresponding to a linear portion of the stress-strain curve; (iii) stable crack growth over the CI and CD interval; and (iv) unstable crack growth over the CD threshold, which leads to failure at the peak stress (i.e., the UCS). The measured UCS ranges between 127 and 158 MPa, with a mean value of 143 MPa, and a standard deviation of 12 MPa. Axial stress-axial strain curves (**Figure 10a**) present a consistent linear portion between 30 and 35% of the UCS. Young's modulus and Poisson's ratio were calculated by deriving the linear stress–strain relationship (see details in Section 3.3.1)

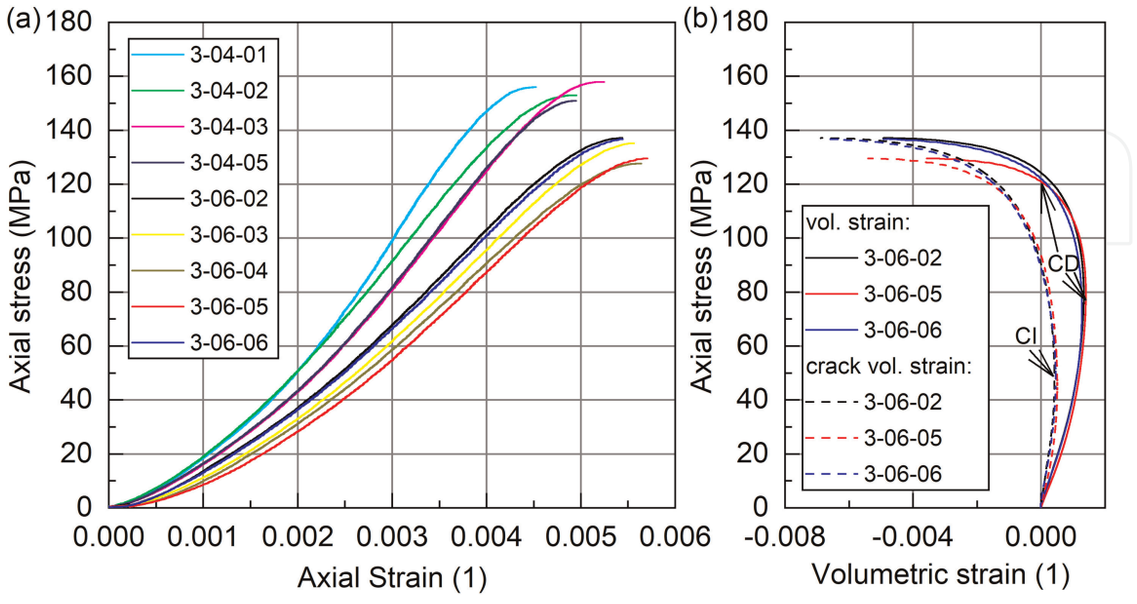

Figure 10.
Axial stress-strain curves derived from uniaxial compression tests on herrnholz granite cylinders in ambient conditions. (a) Axial stress-axial strain curves overloading; (b) Axial stress-volumetric strain curves overloading. CI: crack initiation threshold; CD: crack damage threshold.

over this interval, indicating a mean Young's modulus of 35 GPa, and Poisson's ratio of 0.28 under ambient environmental conditions.

Three of the tested samples were instrumented with a radial chain extensometer (see **Figure 5a**), which allowed for the determination of radial strain, and thus the volumetric strain and crack volumetric strain. The crack volumetric strain reversal method (see in Section 3.3.1) indicates an average CI threshold of 47 ± 1.2MPa (**Figure 10b**), $\sim$ 35% of the UCS, consistent with existing measurements typically between 30 and 35% of the UCS [42, 52–55]. The CD threshold is estimated to fall between 58% UCS and 92% UCS, corresponding to the volumetric strain reversal point [53, 56, 57] and the dilation point (transition of volumetric strain from positive to negative), respectively.

SENB tests demonstrate an exceptionally consistent failure load of 14.54 kN $\pm$ 0.18kN, suggesting a (theoretical) average fracture toughness of 1.82 ± 0.02 MPa $\cdot$ m$^{1/2}$ following Eq. (3). Progressive failure characteristics during the load relaxation phase of one staged test (see test description in Section 3.3.2) were observed through a progressive increase in crack mouth opening displacement when the piston displacement was held at 98% of the predetermined peak load. This, however, requires to be supported by additional tests (e.g., [58]).

4.4 Hydroscopic expansion

Horizontal and vertical expansion in association with water imbibition were observed in two tested Herrnholz granite specimens. **Figure 11** demonstrates the evolution of vertical strains of one tested sample (as an example) during water imbibition. Adopting a compression negative convention in reporting strains, the vertical strains are extensional (**Figure 11**) upon wetting and progress to more than 30 mm below the top surface at the end of wetting (**Figure 11f**).

Heterogeneities observed in the vertical strain field (see **Figure 11**) indicate imbibition occurs along preferential capillary conduits that appear to be oriented parallel to the micro-crack fabric. Although laboratory studies have previously found little variability in the initial (24 h) capillarity of granite containing a population of preferentially oriented micro-cracks, longer-term (38 days) water uptake can be up to 20% greater in the grain-parallel orientation than the rift parallel [13].

Calculated mean linear strain assumed to be $(\epsilon_{\text{vertical}} + 2\epsilon_{\text{horizontal}})/3$, progressively increased with water imbibition in both samples, up to 4.7×10^4, and 4.0×10^4, respectively, at the end of two tests. These strain magnitudes are consistent with those previously documented in association with complete wetting of Hauzenberg granite [29] and other granitic rocks [27, 28]. This suggests that Herrnholz granite specimens behave in a similar manner to these previously tested granitic materials. Hydroscopic expansion observed in other rock types [27, 59, 60] is one (e.g., limestone and marbles) or several (e.g., sandstone) orders of magnitude greater than that observed in Herrnholz granite specimens, which could be associated with mineral composition, pore size distribution, and grain/micro-crack fabric.

4.5 Hygroscopic expansion and elastic weakening

Axial and radial expansion of the Herrnholz granite cylinder subjected to a stepwise increase in relative humidity was observed in both the 'staged' and 'continuous'

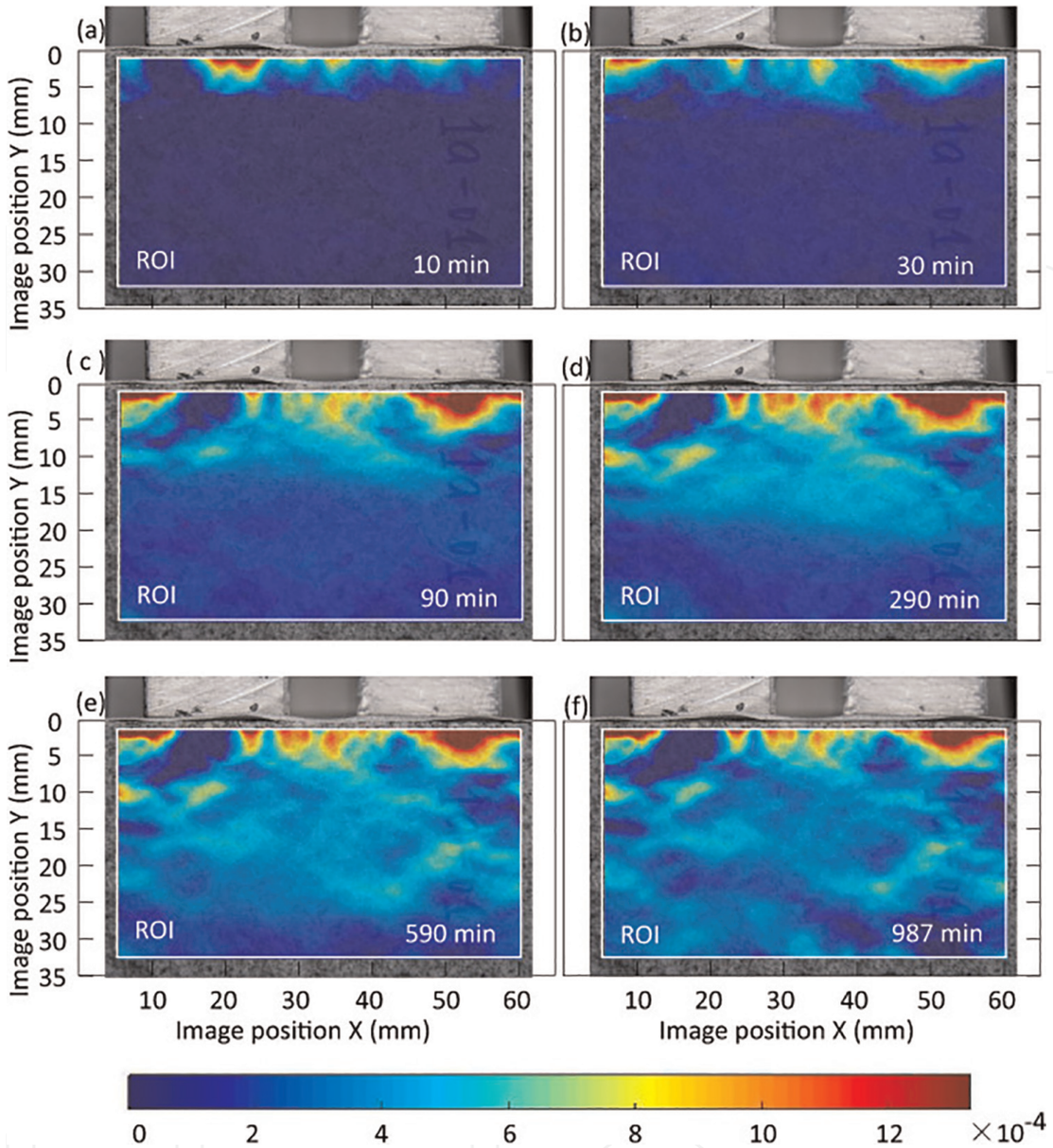

Figure 11.
Vertical strain evolution during water imbibition of a free-standing granite prism.

tests. Strains evolution over the 0.1 MPa hold periods (see test description in Section 3.4.2) provides information on the rock deformation in response to ambient humidity change. As is demonstrated by **Figure 12**, the axial strain during the staged test consistently increased with increasing humidity and typically stabilized after approximately 37 h at each humidity level. The response of radial strain is relatively smaller $\left(\max .2.0 \times 10^4 \text{ vs. } 3.0 \times 10^4\right)$, and it continued to progress throughout each humidity interval. Calculated volumetric strain, assumed to be axial strain $+2\times$ radial strain, during the staged test consistently increased with increasing humidity, up to 3.0×10^4 at the end of the 90% humidity stage. The overall evolution of strains in the staged test compares favorably with that in the continuous test, with the maximum volumetric strain in the continuous test reaching a more-or-less stable peak of 8.0×10^4 at the end of 90% humidity level.

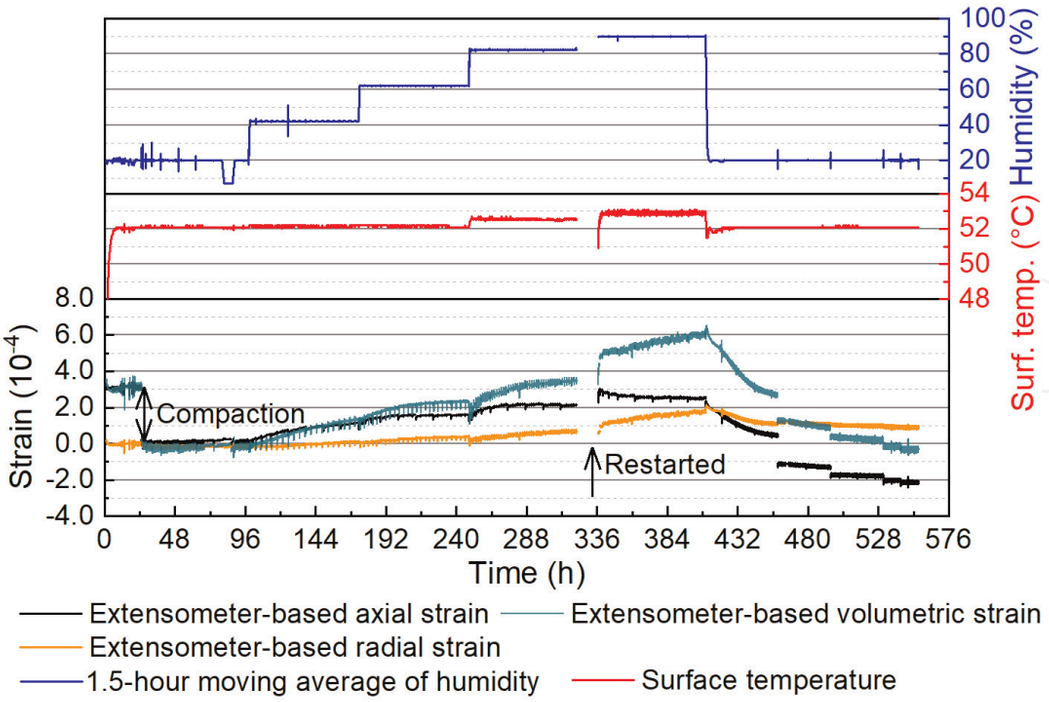

Figure 12.
Temporal evolution of strains (axial, radial, and volumetric) during hold periods across the 20–90% relative humidity range of the staged test.

Young's modulus and Poisson's ratio at varying humidity conditions were derived from axial stress–strain relationships during loading steps (see test description in Section 3.4.2) at each humidity level. Overall, Young's modulus in the staged and continuous tests decreased from ~ 43 to ~ 44 GPa, respectively, down to ~ 38 GPa in response to relative humidity increasing from 20% to 90% (see **Figure 13** for the staged test as an example). Returning humidity to 20% resulted in a recovery of Young's modulus, with a persistent 0.5 GPa increase in stiffness on completion of the staged test, and a similar decrease in stiffness on completion of the continuous test. Poisson's ratio (calculated from the staged test) increased from 0.12 to 0.26 across the humidity range, with a 60% recovery when the humidity level was reduced to 20% (**Figure 13**). Assuming an isotropic medium, bulk modulus from Young's modulus (E) and Poisson's ratio derived by $\frac{E}{3\times(1-2v)}$ increased from 18.8 GPa to 26 GPa, before decreasing to 22 GPa at the completion of the staged test (**Figure 13**).

4.6 Pore size effect on hydroscopic and hygroscopic properties

The deformation and elasticity variations of Herrnholz granite in response to the addition of liquid water or exposure to high humidity conditions have been commonly attributed to the physical process of water vapor adsorption [43, 49]. It exhibits different stages depending on the pore size within the absorbent media. In general, adsorption in micropores (pore diameter < 2 nm based on Ref. [61]) is dominated by the interactions between the adsorbed fluid and pore wall due to the small pore size. Micropore filling is therefore continuous at low relative pressure [61], with a limiting amount adsorbed at the saturation pressure. In contrast, the size of meso- (2 nm $<$ pore diameter < 50 nm based on Ref. [61]) and macropores (pore diameter > 50 nm

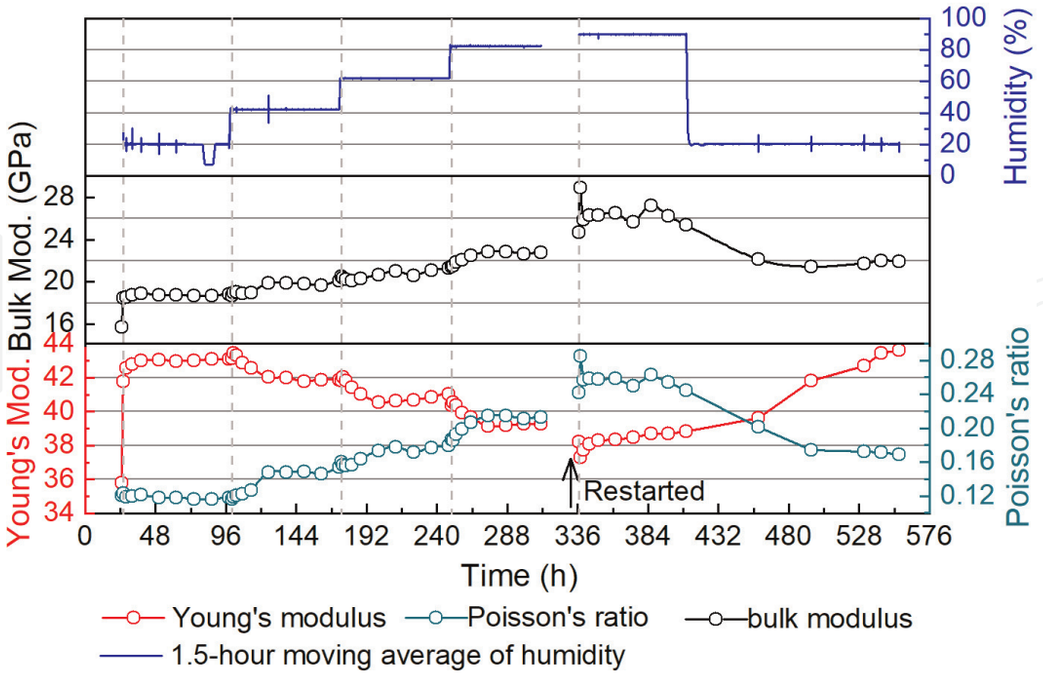

Figure 13.
Temporal evolution of Young's modulus, Poisson ratio, and bulk modulus (calculated from axial stress-strain measurement) for the staged test. The sharp change in Young's modulus immediately after the 1-h hold interval is indicated by dashed vertical lines.

based on Ref. [61]) is significantly larger than the effective range of adsorbent-adsorptive interaction (a few nm). Therefore, adsorption in meso- and macropores depends not only on the fluid-wall attraction, but also on the attractive interactions between the fluid molecules, leading to a sharp increase in the amount of adsorbate as relative pressure increases to a critical level, or even unrestricted monolayer–multilayer formation during adsorption. More precisely, Gor and Neimark [62] developed an adsorption model for mesoporous media, which describes the adsorption stress as a function of environmental conditions, pore size within the absorbent media, and adsorbate–-adsorbent interaction.

Combing the volumetric expansion ($\Delta\epsilon_{vol}$) and changing bulk modulus (K) with the assumption of a linear Hooke law, the adsorption stress ($\sigma_a = K\Delta\epsilon_{vol}$) developed from 'zero' to 25 GPa as relative humidity increases from 20% to 90%, agreeing well with modeled adsorption stress change for cylindrical pores with a characteristic diameter (i.e., 10 nm for Herrnholz granite, see Section 4.1). This model predicts a contrast of adsorption stress of a factor of ~ 2 between the 5 nm diameter and 10 nm diameter pores under the same environmental conditions for water vapor adsorption. We therefore expect larger adsorption-induced strains and elastic variations for intact rock containing smaller micropores or microfractures with smaller apertures.

5. Conclusions

Based on the material characterization results that involve microstructure distribution, acoustic wave velocity, elastic and brittle properties, and hydroscopic and hygroscopic properties, the following conclusions about the Herrnholz granite can be drawn:

1. fine-grained granite with grain sizes ranging from 0.03 to 1 mm (mean 0.23 mm, standard deviation 0.13 mm);

2. mesoporous media with a majority of 10 nm diameter mesopores providing 4.6 m^2/g specific surface areas;

3. isotropic wave propagation along three major splitting directions, with a mean velocity of 3982(±64) m/s;

4. homogeneous material, as evidenced by a high degree of consistency in bulk density, porosity, stress–strain response, and fracture toughness across multiple samples;

5. detectable variations in strains and elastic properties caused by water vapor adsorption, which has not been widely recognized in rock mechanics or earth surface process research.

Acknowledgements

This work was supported by Swiss National Science Foundation (SNSF) R 'Equip "Long-term damage evolution in brittle rocks subject to controlled climatic conditions" (Project 170746) and "Physical constraints on natural and induced earthquakes using innovative lab-scale experiments: The LabQuake Machine" (Project 170766). The authors greatly thank Dr. Michael Plötze for the pore size distribution measurement at the Clay Lab of Institute for Geotechnical Engineering, ETH Zürich, and Markus Rast for the grain density measurement at the Rock Physics and Mechanics Lab, ETH Zürich.

Conflict of interest

The authors declare no conflict of interest.

Abbreviations

UCS	uniaxial compressive strength
SENB	single edge notch bending
DIC	digital image correlation
HQ	Herrnholz quarry
HP	Hauzenberg pluton
BET	Brunauer-Emmett-Teller
CI	crack initiation
CD	crack damage

Physical and Mechanical Properties of Herrnholz Granite: An Ideal Experimental Material
DOI: http://dx.doi.org/10.5992/intechopen.1001093

Author details

Ying Li[1,2*] and Rui Wu[2]

1 Hebei University of Technology, Tianjin, China

2 ETH Zurich, Zürich, Switzerland

*Address all correspondence to: ying.li@erdw.ethz.ch

References

[1] Ramspott LD, Ballou LB, Carlson RC, Montan DN, Butkovich TR, Duncan JE, et al. Technical Concept for Test of Geologic Storage of Spent Reactor Fuel in the Climax Granite, Nevada Test Site. Livermore, CA (United States): California Univ; 1979. Lawrence Livermore Lab. UCID-18197

[2] Gnirk PF, McClain WC. An overview of geologic disposal of radioactive wastes. In: Bergman M, editor. Subsurface Space. Stockholm, Sweden: Pergamon; 1981. pp. 865-872

[3] Miller W, Alexander R, Chapman N, McKinley JC, Smellie JAT. Geological Disposal of Radioactive Wastes and Natural Analogues. Oxford, England: Elsevier; 2000

[4] Park ES, Jung YB, Song WK, Lee DH, Chung SK. Pilot study on the underground lined rock cavern for LNG storage. Engineering Geology. 2010; **116**(1):44-52

[5] Reid JC, Myers C, Carpenter RH. underground storage of refrigerated natural gas in granites of the Southeastern US. In: 47th Annual AAPG-SPE Eastern Section Joint Meeting, Pittsburgh, Pennsylvania

[6] Sibbitt WL, Dodson JG, Tester JW. Thermal conductivity of crystalline rocks associated with energy extraction from hot dry rock geothermal systems. Journal of Geophysical Research. 1979; **84**:1117-1124

[7] Kumari WGP, Ranjith PG, Perera MSA, Shao S, Chen BK, Lashin A, et al. Mechanical behaviour of Australian Strathbogie granite under in-situ stress and temperature conditions: An application to geothermal energy extraction. Geothermics. 2017;**65**:44-59

[8] Brunton GD, McClain WC. Geological Criteria for Radioactive Waste Repositories. Oak Ridge, Tenn. (USA): Union Carbide Corp; 1977. Office of Waste Isolation; Y/OWI/TM-47

[9] Tarkowski R. Underground hydrogen storage: Characteristics and prospects. Renewable and Sustainable Energy Reviews. 2019;**105**:86-94

[10] Matos CR, Carneiro JF, Silva PP. Overview of large-scale underground energy storage Technologies for Integration of renewable energies and criteria for reservoir identification. Journal of Energy Storage. 2019;**21**: 241-258

[11] Freire-Lista D, Fort R. Causes of scaling on bush-hammered heritage ashlars: A case study—Plaza Mayor of Madrid (Spain). Environmental Earth Sciences. 2016;**75**(10):1-12

[12] Freire-Lista DM, Fort R, Varas-Muriel MJ. Thermal stress-induced microcracking in building granite. Engineering Geology. 2016;**206**:83-93

[13] Freire-Lista D, Fort R. Exfoliation microcracks in building granite. Implications for anisotropy. Engineering Geology. 2017;**220**:85-93

[14] Sousa LMO. Petrophysical properties and durability of granites employed as building stone: A comprehensive evaluation. Bulletin of Engineering Geology and the Environment. 2014; **73**(2):569-588

[15] Sousa LMO, Suárez del Río LM, Calleja L, Ruiz de Argandoña VG, Rey AR. Influence of microfractures and porosity on the physico-mechanical properties and weathering of ornamental

granites. Engineering Geology. 2005; **77**(1):153-168

[16] Sousa LMO. The influence of the characteristics of quartz and mineral deterioration on the strength of granitic dimensional stones. Environment and Earth Science. 2013; **69**(4):1333-1346

[17] Dwivedi RD, Goel RK, Prasad VVR, Sinha A. Thermo-mechanical properties of Indian and other granites. International Journal of Rock Mechanics and Mining Sciences. 2008;**45**(3): 303-315

[18] David C, Menéndez B, Darot M. Influence of stress-induced and thermal cracking on physical properties and microstructure of La Peyratte granite. International Journal of Rock Mechanics and Mining Sciences. 1999;**36**(4): 433-448

[19] Heuze FE. High-temperature mechanical, physical and thermal properties of granitic rocks—A review. International Journal of Rock Mechanics and Mining Sciences & Geomechanics Abstracts. 1983;**20**(1):3-10

[20] Shao S, Wasantha PLP, Ranjith PG, Chen BK. Effect of cooling rate on the mechanical behavior of heated Strathbogie granite with different grain sizes. International Journal of Rock Mechanics and Mining Sciences. 2014; **70**:381-387

[21] Vázquez P, Shushakova V, Gómez-Heras M. Influence of mineralogy on granite decay induced by temperature increase: Experimental observations and stress simulation. Engineering Geology. 2015;**189**:58-67

[22] Vasconcelos G, Lourenço PB, Alves CAS, Pamplona J. Ultrasonic evaluation of the physical and mechanical properties of granites. Ultrasonics. 2008;**48**(5):453-466

[23] Cerrillo C, Jiménez A, Rufo M, Paniagua J, Pachón FT. New contributions to granite characterization by ultrasonic testing. Ultrasonics. 2014; **54**(1):156-167

[24] Korobiichuk I, Korobiichuk V, Hajek P, Kokes P, Juś A, Szewczyk R. Investigation of leznikovskiy granite by ultrasonic methods. Archives of Mining Sciences. 2018;**63**(1):75-82

[25] Vasconcelos G, Lourenço PB, Alves C, Pamplona J. Prediction of the Mechanical Properties of Granites by Ultrasonic Pulse Velocity and Schmidt Hammer Hardness. Luis, Missouri. 2007

[26] Ericson K. Geomorphological surfaces of different age and origin in granite landscapes: An evaluation of the Schmidt hammer test. Earth Surface Processes and Landforms. 2004;**29**(4): 495-509

[27] Hockman A, Kessler DW. Thermal and moisture expansion studies of some domestic granites. US Bureau Standards of Journal Research. 1950;**44**:395-410

[28] Swanson PL. Subcritical crack growth and other time-and environment-dependent behavior in crustal rocks. Journal of Geophysical Research: Solid Earth. 1984;**89**(B6): 4137-4152

[29] Schult A, Shi G. Hydration swelling of crystalline rocks. Geophysical Journal International. 1997;**131**(1):179-186

[30] Rivas T, Prieto B, Silva B. Influence of rift and bedding plane on the physico-mechanical properties of granitic rocks. Implications for the deterioration of

granitic monuments. Building and Environment. 2000;**35**(5):387-396

[31] Lindqvist JE, Åkesson U, Malaga K. Microstructure and functional properties of rock materials. Materials Characterization. 2007;**58**(11):1183-1188

[32] Nasseri MHB, Mohanty B. Fracture toughness anisotropy in granitic rocks. International Journal of Rock Mechanics and Mining Sciences. 2008;**45**(2): 167-193

[33] Klein T, Kiehm S, Siebel W, Shang C, Rohrmüller J, Dörr W, et al. Age and emplacement of late-Variscan granites of the western Bohemian Massif with main focus on the Hauzenberg granitoids (European Variscides, Germany). Lithos. 2008;**102**(3–4):478-507

[34] Siebel W, Shang C, Reitter E, Rohrmüller J, Breiter K. Two distinctive granite suites in the SW Bohemian Massif and their record of emplacement: Constraints from geochemistry and zircon 207Pb/206Pb chronology. Journal of Petrology. 2008;**49**(10):1853-1872

[35] Brunauer S, Emmett PH, Teller E. Adsorption of gases in multimolecular layers. Journal of the American Chemical Society. 1938;**60**(2):309-319

[36] Barrett EP, Joyner LG, Halenda PP. The determination of pore volume and area distributions in porous substances. I. Computations from nitrogen isotherms. Journal of the American Chemical Society. 1951;**73**(1):373-380

[37] Selvadurai PA, Wu R, Bianchi P, Niu Z, Michail S, Madonna C, et al. A methodology for reconstructing source properties of a conical piezoelectric actuator using Array-based methods. Journal of Nondestructive Evaluation. 2022;**41**(1):23

[38] Wu R, Selvadurai PA, Chen C, Moradian O. Revisiting piezoelectric sensor calibration methods using elastodynamic body waves. Journal of Nondestructive Evaluation. 2021;**40**(3):68

[39] Martiartu NK, Böhm C. TTomo: Straight ray tomography. Seismology and Wave Physics group at ETH Zurich; 2017. Available from: https://cos.ethz.ch/software/research/ttomo.html

[40] Li Y, Leith K, Moradian O, Loew S, Perras MA. A new laboratory to undertake climatically controlled static loading and constant strain tests: Design and preliminary results. In: 53rd US Rock Mechanics/Geomechanics Symposium. New York City, New York: OnePetro; 2019

[41] Diederichs MS, Martin CD. Measurement of spalling parameters from laboratory testing. In: Rock Mechanics and Environmental Engineering. Paper presented at European Rock Mechanics Symposium. Lausanne, Switzerland. 2010. pp. 323-326

[42] Martin CD. The Strength of Massive Lac du Bonnet Granite around Underground Openings. Canada: Ph.D University of Manitoba; 1993

[43] Li Y, Leith K, Perras MA, Loew S. Digital image correlation–based analysis of hygroscopic expansion in Herrnholz granite. International Journal of Rock Mechanics and Mining Sciences. 2021; **146**:104859

[44] Baud P, Zhu W, Wong T. Failure mode and weakening effect of water on sandstone. Journal of Geophysical Research: Solid Earth. 2000;**105**(B7): 16371-16389

[45] Chang C, Haimson B. Effect of fluid pressure on rock compressive failure in a

nearly impermeable crystalline rock: Implication on mechanism of borehole breakouts. Engineering Geology. 2007; **89**(3):230-242

[46] Rajabzadeh MA, Moosavinasab Z, Rakhshandehroo G. Effects of rock classes and porosity on the relation between uniaxial compressive strength and some rock properties for carbonate rocks. Rock Mechanics and Rock Engineering. 2012;**45**(1):113-122

[47] Nicolas A, Fortin J, Regnet J, Dimanov A, Guéguen Y. Brittle and semi-brittle behaviours of a carbonate rock: Influence of water and temperature. Geophysical Journal International. 2016;**206**(1):438-456

[48] Heap MJ, Farquharson JI, Kushnir ARL, Lavallée Y, Baud P, Gilg HA, et al. The influence of water on the strength of Neapolitan yellow tuff, the most widely used building stone in Naples (Italy). Bulletin of Volcanology. 2018;**80**(6):51

[49] Li Y, Leith K, Perras MA, Loew S. Effect of ambient humidity on the elasticity and deformation of unweathered granite. Journal of Geophysical Research [Solid Earth]. 2022;**127**(11):1-27

[50] Blaber J, Adair B, Antoniou A. Ncorr: Open-source 2D digital image correlation matlab software. Experimental Mechanics. 2015;**55**(6):1105-1122

[51] Labani MM, Rezaee R, Saeedi A, Al HA. Evaluation of pore size spectrum of gas shale reservoirs using low pressure nitrogen adsorption, gas expansion and mercury porosimetry: A case study from the Perth and Canning Basins, Western Australia. Journal of Petroleum Science and Engineering. 2013;**112**:7-16

[52] Brace W, Paulding B Jr, Scholz C. Dilatancy in the fracture of crystalline rocks. Journal of Geophysical Research. 1966;**71**(16):3939-3953

[53] Martin CD. Seventeenth Canadian geotechnical colloquium: The effect of cohesion loss and stress path on brittle rock strength. Canadian Geotechnical Journal. 1997;**34**(5):698-725

[54] Katz O, Reches Z. Microfracturing, damage, and failure of brittle granites: Microfracturing and failure of granites. Journal of Geophysical Research. 2004; **109**(B1)

[55] Nicksiar M, Martin CD. Evaluation of methods for determining crack initiation in compression tests on low-porosity rocks. Rock Mechanics and Rock Engineering. 2012;**45**(4):607-617

[56] Bieniawski ZT. Mechanism of brittle fracture of rock: Part I—Theory of the fracture process. International Journal of Rock Mechanics and Mining Sciences & Geomechanics Abstracts. 1967;**4**(4): 395-406

[57] Lajtai EZ. Brittle fracture in compression. International Journal of Fracture. 1974;**10**(4):525-536

[58] Moradian O, Wu R, Li Y, Leith K, Loew S. Acoustic emission and digital image correlation for damage evolution in brittle rocks under time-dependent tensile loading. In: IOP Conference Series: Earth and Environmental Science. Vol. 833. Turin, Italy: IOP Publishing; 2021. p. 012090

[59] Weiss T, Siegesmund S, Kirchner D, Sippel J. Insolation weathering and hygric dilatation: Two competitive factors in stone degradation. Environmental Geology. 2004;**46**(3): 402-413

[60] Koch A, Siegesmund S. The combined effect of moisture and temperature on the anomalous expansion behaviour of marble. Environmental Geology. 2004;**46**(3): 350-363

[61] Gregg S. Adsorption, Surface Area and Porosity. 2nd ed. London: Academic Press; 1982

[62] Gor GY, Neimark AV. Adsorption-induced deformation of mesoporous solids. Langmuir. 2010;**26**(16): 13021-13027